iScience

CellPress

Article

Nanoengineered Metasurface Immunosensor with over 1000-Fold Electrochemiluminescence Enhancement for Ultra-sensitive Bioassay

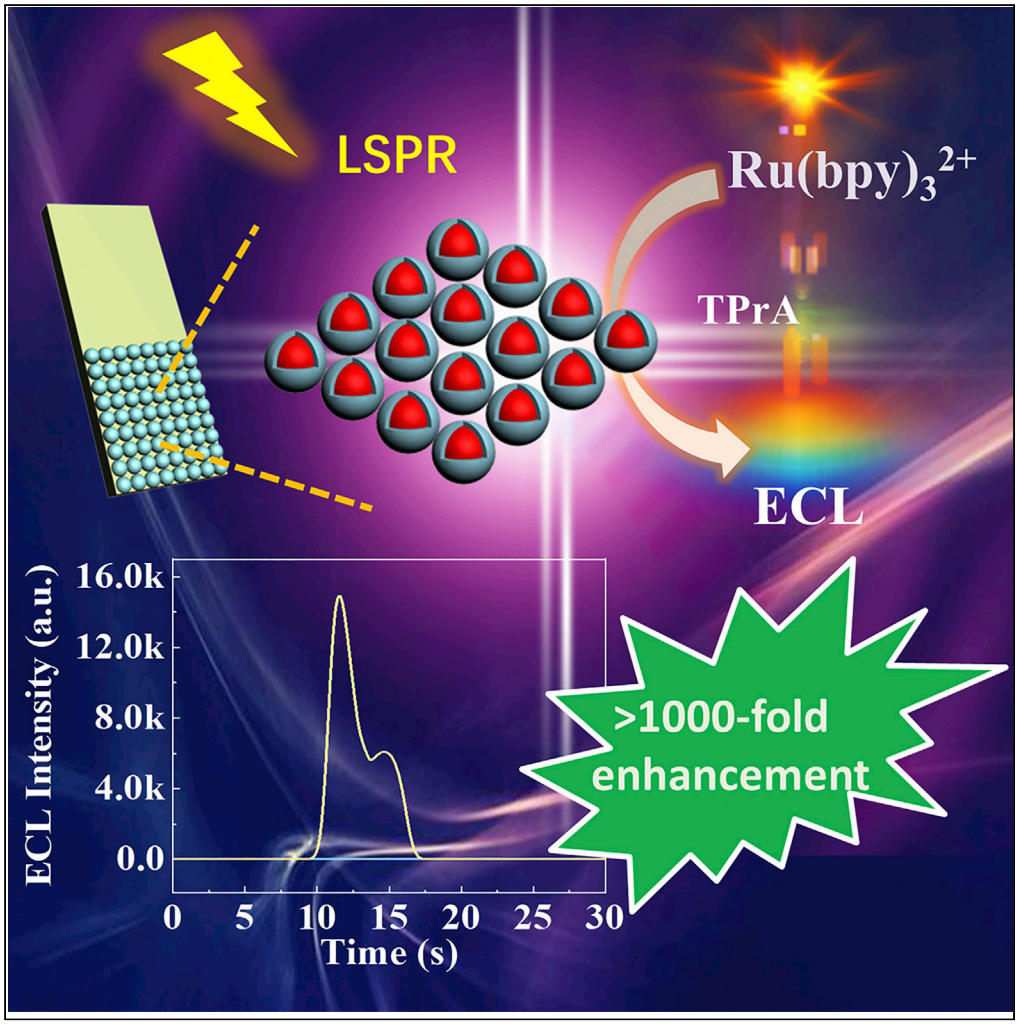

Chuanping Li, Shanshan Wang, Haijuan Li, Muhammad Saqib, Chen Xu, Yongdong Jin

ydjin@ciac.ac.cn

HIGHLIGHTS

A unique Au@SiO_2 NP-based 2D metamaterial was constructed

The plasmon effects were fully utilized to enhance ECL excitation

The as-fabricated metasurfaced ECL electrode shows over 1,000-fold enhancement

Li et al., iScience 17, 267–276
July 26, 2019
https://doi.org/10.1016/j.isci.2019.06.042

iScience

CellPress

Article

Nanoengineered Metasurface Immunosensor with over 1000-Fold Electrochemiluminescence Enhancement for Ultra-sensitive Bioassay

Chuanping Li,[1,2,4,5] Shanshan Wang,[1,3,5] Haijuan Li,[1] Muhammad Saqib,[1] Chen Xu,[1] and Yongdong Jin[1,2,6,*]

SUMMARY

Enhancing electrochemiluminescence (ECL) with plasmonic materials is promising but still a long-standing barrier to improve its sensitivity for ultrasensitive bioassays, due to the lack of comprehensive understanding and effective strategies to fully utilize plasmonic effects for ECL enhancement. Herein, by insulating gold nanoparticles with silica shells (Au@SiO_2 NPs), and finely tuning their core/shell sizes and controlling interparticle spacing via assembling them into a dense nanomembrane, we develop a novel 2D metasurface. Due to well-controlled high density "hot spots" and 2D ordered arrangement of the unit NPs in the nanomembrane, the metasurfaced ECL electrode shows over 1,000-fold plasmonic ECL enhancement for the classical $Ru(bpy)_3^{2+}$-tripropylamine system, which is two orders of magnitude higher than ever reported (<30-fold). Such fabricated ECL biosensor demonstrates superior detection performance for prostate-specific antigen with a detection limit of 3 fg mL^{-1}. Our results provide understanding of plasmonic effects for ECL enhancement and will benefit for biosensor construction for ultrasensitive bioassays.

INTRODUCTION

Electrochemiluminescence (ECL) is the emission from an excited luminophore generated by an electrochemical redox reaction (Hu and Xu, 2010; Liu et al., 2015; Miao, 2008; Richter, 2004). In recent years, high-throughput, miniaturized biosensors based on ECL technology that are capable of multiplexing detection with high sensitivity, low detection limit, and good selectivity have become very powerful analytical methods and have been widely used in immunoassay and medical diagnostics. Although significant progresses have been achieved over the past decades, the mechanisms of ECL still need to be further studied and its detection sensitivity needs to be further improved for ultrasensitive bioassays (Wu et al., 2014). As an attractive solution, surface-enhanced electrochemiluminescence (SEECL) (Wang et al., 2015a), which merges photonics with photoelectronics at the nanoscale and provides an effective avenue to increase the sensitivity, has attracted enormous attention in the development of next-generation ECL biosensors.

Usually, localized surface plasmon resonance (LSPR) in plasmonic nanostructures can improve the sensitivity of SEECL biosensors via two main pathways: photonic enhancement and plasmon-induced energy transfer (PIRET) enhancement (Li et al., 2013; Wang et al., 2015a; Wu, 2018). For mostly reported regular or patterned plasmonic nanostructures, the light emitted by the luminescent molecule (e.g., $Ru(bpy)_3^{2+}$) under the excitation of electricity is efficiently scattered multiple times, which increases the optical path length and photon flux in the luminescent molecules (Wu, 2018). This is referred to as photonic enhancement (or resonant light scattering), which contributes to the enhancement of ECL signals. In contrast, PIRET enhancement proceeds via a non-radiative process that is based on the near-field dipole-dipole interaction between the plasmonic nanostructures and the luminescent molecule. The PIRET does not require direct contact or band alignment; instead, the ECL efficiency is determined by the spectral overlap between the luminescent molecules' emission band edge and the LSPR absorbance (Li et al., 2013; Wu, 2018). Since the first report on surface plasmon-coupled ECL in 2004 (Zhang et al., 2004), Guo and Xu et al. have developed multiple strategies to fabricate SEECL systems based on the energy resonance transfer between $Ru(bpy)_3^{2+}$ and plasmonic nanoparticles (NPs), or between fluorescent quantum dot and plasmonic NPs, which greatly promoted the development of SEECL systems for ultrasensitive biodetections (Li et al., 2016, 2018; Lu et al., 2018; Wang et al., 2011, 2015b).

Although some progresses have been made in this field, the development of plasmonic SEECL biosensors is still severely hindered by the lack of comprehensive understanding of the underlying enhancement

[1]State Key Laboratory of Electroanalytical Chemistry, Changchun Institute of Applied Chemistry, Chinese Academy of Sciences, 5625 Renmin Street, Changchun 130022, P. R. China

[2]University of Chinese Academy of Sciences, Beijing 100049, P. R. China

[3]College of Chemistry, Liaoning University, Shenyang 110036, P. R. China

[4]Present address: College of Biological and Chemical Engineering, Anhui Polytechnic University, Wuhu 241000, P. R. China

[5]These authors contributed equally

[6]Lead Contact

*Correspondence: ydjin@ciac.ac.cn

https://doi.org/10.1016/j.isci.2019.06.042

mechanisms and the corresponding strategies and methods to finely construct effective electrode interfaces and materials, and final sensors. Due to the lack of proper fabrication method and interfacial nanoengineering strategy, the resulting interfaces of electrodes were less effective and uncontrollable. Thus, in many cases, although plasmonic nanostructures had been optimized to achieve strong coupling with luminescent molecules, the plasmon effects cannot be fully utilized to enhance maximally the ECL because of the disorders of plasmonic nanostructures on the electrode surface, which dramatically weakened the photonic enhancement effect (Li et al., 2016; Wang et al., 2015a). Therefore, only a low enhancement in SEECL (less than ~30-fold) has been achieved so far, and it remains a significant challenge to develop highly efficient SEECL systems for ultrasensitive bioassays and detections.

In this study, we finely fabricated the Au@SiO_2 NP-based layered metamaterial and exploited it as a plasmonically active electrode material for SEECL and biosensing applications. By aqueous-phase core/shell nanoengineering of the unit Au@SiO_2 NPs to finely tune the plasmonic coupling or effects and finally floating transfer the as-prepared ordered metamaterial onto the surface of an indium tin oxide (ITO) electrode, the resulting metasurfaced ECL electrode enhances significantly the ECL signals (over 1,000-fold) because of the synergy effect of photonic enhancement and PIRET. Locally, the abundance of finely controlled silica nanogaps in the dense nanomembrane creates rich "hot spots" and leads to significant enhancement of electromagnetic (EM) fields, which increases the plasmon coupling through PIRET (Jain et al., 2008; Lin et al., 2015; Shin et al., 2015). Moreover, the 2D order of the metamaterial and large size of AuNPs used (typically ~75 nm in diameter) will benefit for the scattering of the incident light and "light trapping" of luminescent molecules, leading to an increase in photon flux and excitation efficiency in the luminescent molecules (Li et al., 2013; Wu, 2018). By varying the silica-shell thicknesses and AuNP sizes, the platform allows us to systematically probe the photonic enhancement and PIRET enhancement mechanisms and their effects on performances of SEECL sensors. Very impressively, by full exploitation and utilization of plasmonic effects via nanoengineering, the ECL signal was significantly improved with over 1,000-fold enhancement for the classical $Ru(bpy)_3^{2+}$-tripropylamine (TPrA) ECL system, which is the highest ECL enhancement ever reported. For further practical use, a sandwich-type prostate-specific antigen (PSA) immunosensor was also constructed, in which $Ru(bpy)_3^{2+}$-doped SiO_2 (Ru@SiO_2) NPs act as ECL luminophores, and the two kinds of antibodies specific to PSA are modified on the surface of the SEECL electrode and Ru@SiO_2 NPs, respectively. In the presence of PSA, a sandwiched nanoarchitecture of Ru@SiO_2-SEECL electrode is formed. The fabricated ECL immunosensor showed a very low detection limit of 3 fg mL^{-1} for PSA, demonstrating superior detection performance of the metasurfaced SEECL platform for ultrasensitive biodetections.

RESULTS

As reported previously (Li et al., 2013, 2017; Wu, 2018), LSPR-induced electromagnetic (EM) field enhancement around the plasmonic nanostructures can efficiently improve the excitation efficiency of the adjacent luminescent molecule via a non-radiative process. Meanwhile, for regular or patterned plasmonic NPs, the light emitted by the luminescent molecule can efficiently scatter multiple times and increase the photon flux in the luminescent molecules. Therefore, we expected that the ordered close-packed Au@SiO_2 NP-based monolayered metamaterial can efficiently improve the excitation of the luminescent molecule and enhance the ECL intensity tremendously over the plasmonic nanostructure. Bearing this in mind, we began our studies with a hypothesis-driven strategy by using finite difference time domain (FDTD) simulations to explore the EM enhancement and light-scattering properties of the ordered 2D plasmonic metamaterial of Au@SiO_2. As clearly shown in Figure 1A, significant EM field enhancement of the monolayered 75-nm Au@21.5 nm SiO_2 (up to 15-fold) can be locally generated under plasmonic excitation. Simultaneously, with the decrease of the Au cores (keep the silica shells as 21.5 nm), the EM field intensity reduced gradually (Figures 1B and 1C). In addition, due to the dense structure of the metamaterial, the simulated electric field distribution showed a high density of "hot spots" in the nanogaps between two adjacent Au@SiO_2 NPs (Figures 1A–1C). These super-enhancing locations (hot spots), with ~4-fold larger $|E|^2$ values of the metamaterial than that of discrete NPs (Figure 1D), enhance significantly the EM field. All these simulated results presented above indicated that close-packed 75-nm Au@21.5 nm SiO_2 NP-based monolayered metamaterial had superior EM field enhancement performance and LSPR coupling (collective wave-like charge density fluctuation and surfing of electrons) over dispersed nanostructures. As large nanocrystals or patterned plasmonic structures are also powerful scatterers, the re-radiation of the metasurface (the surface version of metamaterial, typically fabricated artificial materials via suitable periodic arrangement of micro/nanostructured metallic or dielectric inclusions) (Burokur et al., 2010) and light scattering

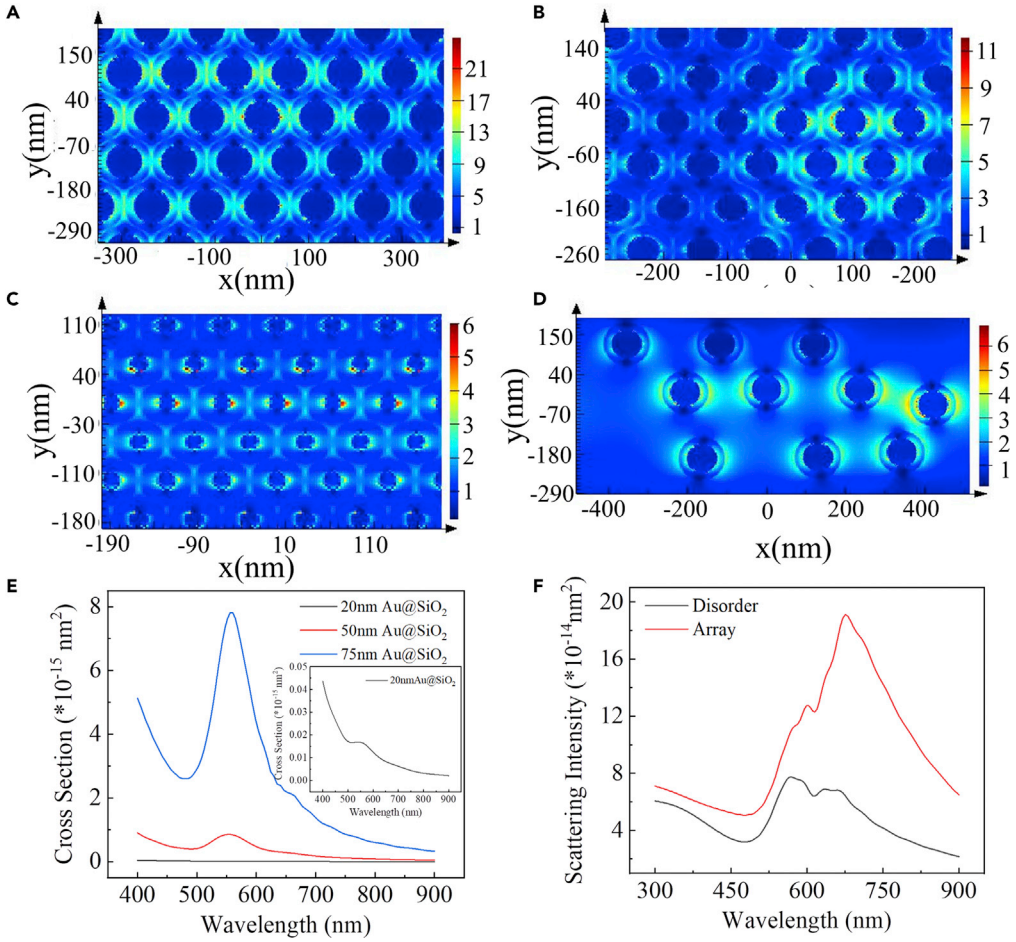

Figure 1. Theoretical Simulation of the 2D Au@SiO_2 NP-Assembled Metasurface

(A–D) (A) FDTD electromagnetic field simulation of 75-nm Au@21.5 nm SiO_2 monolayered metasurface. FDTD electromagnetic field simulation of (B) 50-nm Au@21.5 nm SiO_2, (C) 20-nm Au@21.5 nm SiO_2, and (D) dispersive 75-nm Au@21.5 nm SiO_2 nanoparticle-fabricated nanomembrane.

(E) Simulated scattering cross-sectional spectra of 20-nm Au@21.5 nm SiO_2NPs, 50-nm Au@21.5 nm SiO_2NPs, and 75-nm Au@21.5 nm SiO_2NPs. Inset: enlarged scattering cross-sectional spectra of 20-nm Au@21.5 nm SiO_2NPs.

(F) Simulated scattering intensity spectra of monolayered 75-nm Au@21.5 nm SiO_2NP arrays and disorderly stacked 75-nm Au@21.5 nm SiO_2NPs.

(photonic enhancement) may be another advantage, compared with disordered morphologies (Li et al., 2013; Wu, 2018). As clearly seen in Figure 1E, the simulated scattering cross section dramatically augmented with the increase of the AuNPs' size; furthermore, the 2D well-organized metasurface has large aspect ratio and is favorable for light scattering. Thus, the scattering intensity of the ordered metasurface (Figure 1F) is much stronger than that of the disordered structures; this elastic scattering by plasmons is the source of the EM enhancement contribution, and the enhanced re-radiated dipolar fields in turn excite the luminescent molecules (Atwater and Polman, 2010; Li et al., 2013). According to the above simulation results, we reasoned that the 2D well-organized plasmonic metasurface might demonstrate promising characteristics as ECL electrode for ultrasensitive detection of biomolecular.

We then carried out proof of concept by preparing uniform Au@SiO_2 NPs with controllable shell thicknesses (Figure 2A, please see "Transparent Methods" in the Supplemental Information). By controlling the pH and reaction time, the silica shell thicknesses can be adjusted from 4.0 ± 0.8 nm to 24.6± 2.7 nm (Figures 2B–2G and S1, mean ± transmission electron microscopy [TEM]). With the increase of silica shell thicknesses, the LSPR peak of the particles redshifted gradually (Figure S2). The free-standing monolayered Au@SiO_2 nanomembrane (layered metamaterial) was then fabricated by the liquid-liquid interface self-assembly (LLISA)

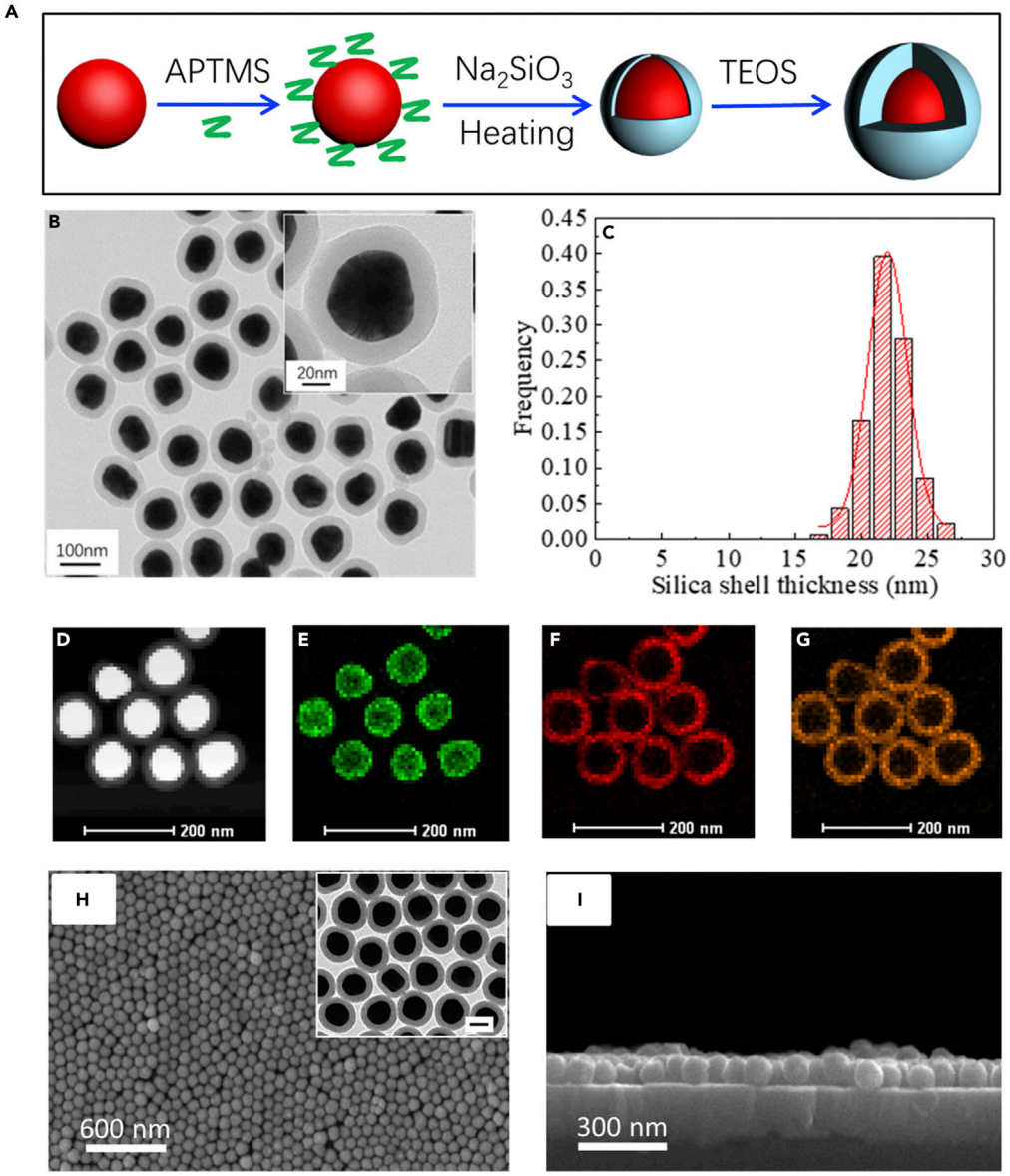

Figure 2. Preparation and Characterizations of the Au@SiO_2 NPs and 2D Metamaterial

(A) The preparation process of Au@SiO_2 NPs.

(B–G) (B) Transmission electron microscopic image, (C) silica shell thickness distribution, and (D) high-angle annular dark-field scanning transmission electron microscopic and (E–G) the corresponding energy-dispersive X-ray spectroscopic elemental mappings of 75-nm Au@21.5 nm SiO_2 NPs. (E) Au, (F) Si, (G) O. Data are represented as mean ± transmission electron microscopy (TEM).

(H and I) Top- and side-view SEM images of the monolayered Au@SiO_2 nanomembrane-assembled metasurface on ITO glasses. (H) Top view, (I) Side view. Inset in (H): transmission electron microscopic image of monolayered Au@SiO_2 nanomembrane.

Scale bar in inset, 50 nm. See also Figures S1–S3.

method. Briefly, colloidal Au@SiO_2 NPs were added in a plastic container and then hexane was poured on top of the colloidal solution; the Au@SiO_2 NPs were subsequently forced to assemble at hexane-water interface after methanol was rapidly added into the colloidal solution. Upon evaporation of hexane, a uniform monolayer of Au@SiO_2 NPs was spontaneously formed over a large area (~several square centimeters). Figure S3 shows photographs and optical images of the resulting nanomembrane after LLISA of the unit Au@SiO_2 NPs, which presents impressively bright golden yellow color at the air-water interface. To fabricate an ECL

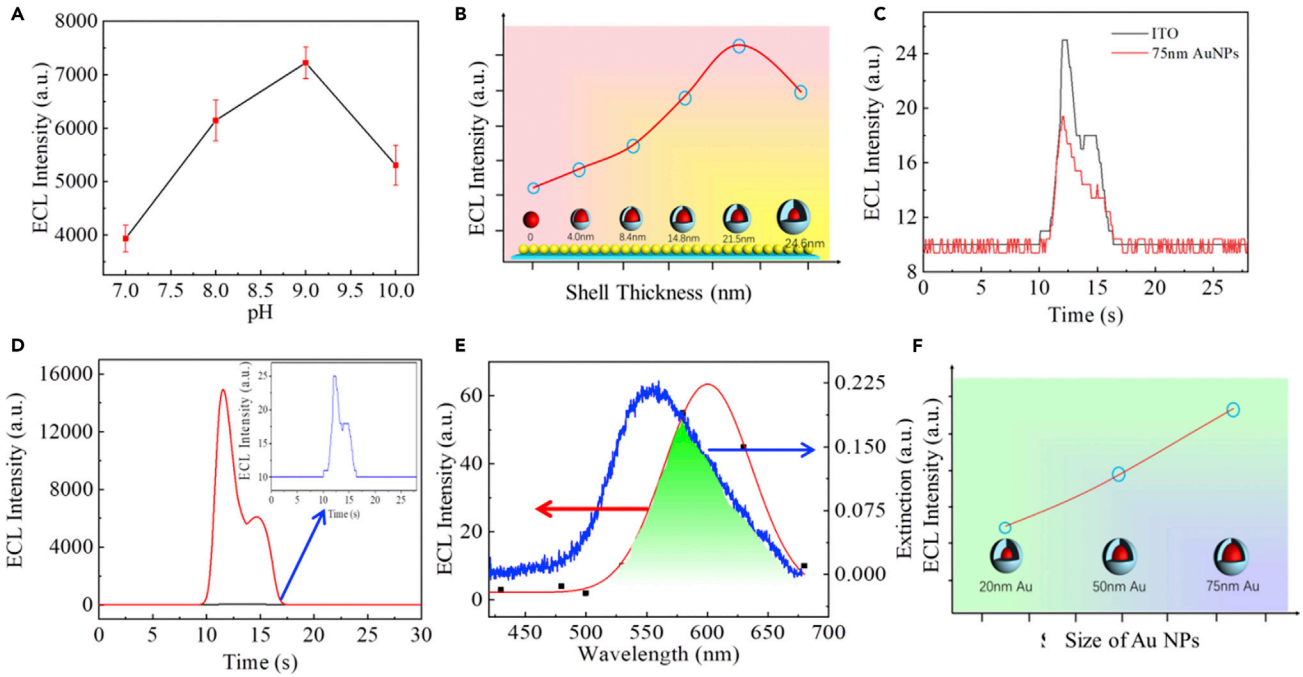

Figure 3. Performance of MASNE in $Ru(bpy)_3^{2+}$-Based Plasmonic ECL System

(A) The effect of pH value of the solution on ECL of the 75-nm Au@21.5 nm SiO_2-modified MASNE with 0.1 M PBS containing 20 μM $Ru(bpy)_3^{2+}$ and 0.1 mM tripropylamine (TPrA).

(B) The effect of silica shell thicknesses on the ECL intensity. Comparison of ECL intensity between ITO and MASNE electrodes at the same concentration of $Ru(bpy)_3^{2+}$-based ECL system (0.1 M PBS solution [pH = 9] containing 20 μmol L^{-1} $Ru(bpy)_3^{2+}$ and 0.1 mmol L^{-1} TPrA).

(C) ECL intensity of the bare AuNP monolayer-based electrode and bare ITO electrode.

(D) Comparison of ECL intensity of MASNE and bare ITO electrode in $Ru(bpy)_3^{2+}$-based plasmonic ECL system. Inset: enlarged image of ECL intensity of bare ITO electrode.

(E) Spectra overlap between the emission spectrum of $Ru(bpy)_3^{2+}$ and extinction spectrum of 75-nm Au@21.5 nm SiO_2-based nanomembrane.

(F) The effect of size of AuNPs (keep the silica shell thicknesses constant, ~21.5 nm) on the ECL intensity.

See also Figures S4–S16.

electrode, the freshly prepared Au@SiO_2 nanomembrane was transferred onto an ITO electrode by the method of floating transfer. As clearly seen from the scanning electron microscopic (SEM) top-/side-view images of the nanomembrane (Figures 2H and 2I), the unit Au@SiO_2 NPs with uniform size were assembled into a dense monolayer nanomembrane with hexagonal close packing, which is beneficial to the photonic scattering and collective wave-like charge density fluctuation (Li et al., 2013; Wu, 2018).

DISCUSSION

To investigate the ECL performance of the nanomembrane, a metasurfaced electrode for the $Ru(bpy)_3^{2+}$-ECL system was constructed. As seen from Figures 3A and S4, the ECL of our system showed the highest intensity at an optimal pH of 9, and therefore the subsequent experiments were performed at the same conditions. Impressively, the as-fabricated monolayer Au@SiO_2 nanomembrane electrode (MASNE) showed much higher ECL intensity compared with the bare ITO electrode (the effective surface areas of ITO electrodes are kept constant, 4 mm × 5 mm). Figures 3B and S5 shows the typical ECL responses of the metasurfaced MASNE system constructed from the 75-nm AuNPs with varied silica shell thickness ranging from 4.0 to 24.6 nm, recorded in the same ECL solution containing 20 μmol L^{-1} $Ru(bpy)_3^{2+}$ and 0.1 mmol L^{-1} TPrA. As a comparison, a slight decrease in ECL response was observed after the decoration of the ITO electrode with monolayer (silica shell-free) AuNP nanomembrane (Figure 3C). The decrease in ECL is attributed to the energy transfer between $Ru(bpy)_3^{2+}$ and bare AuNPs. In the presence of bare AuNPs, the excited $Ru(bpy)_3^{2+}$* transfers the energy to AuNPs in a non-radiative way, and therefore partial ECL quenching was observed (Jebb et al., 2007; Wang et al., 2015a). However, this kind of non-radiative energy transfer can be effectively prevented after the coating of AuNPs with nanoscale insulating SiO_2.

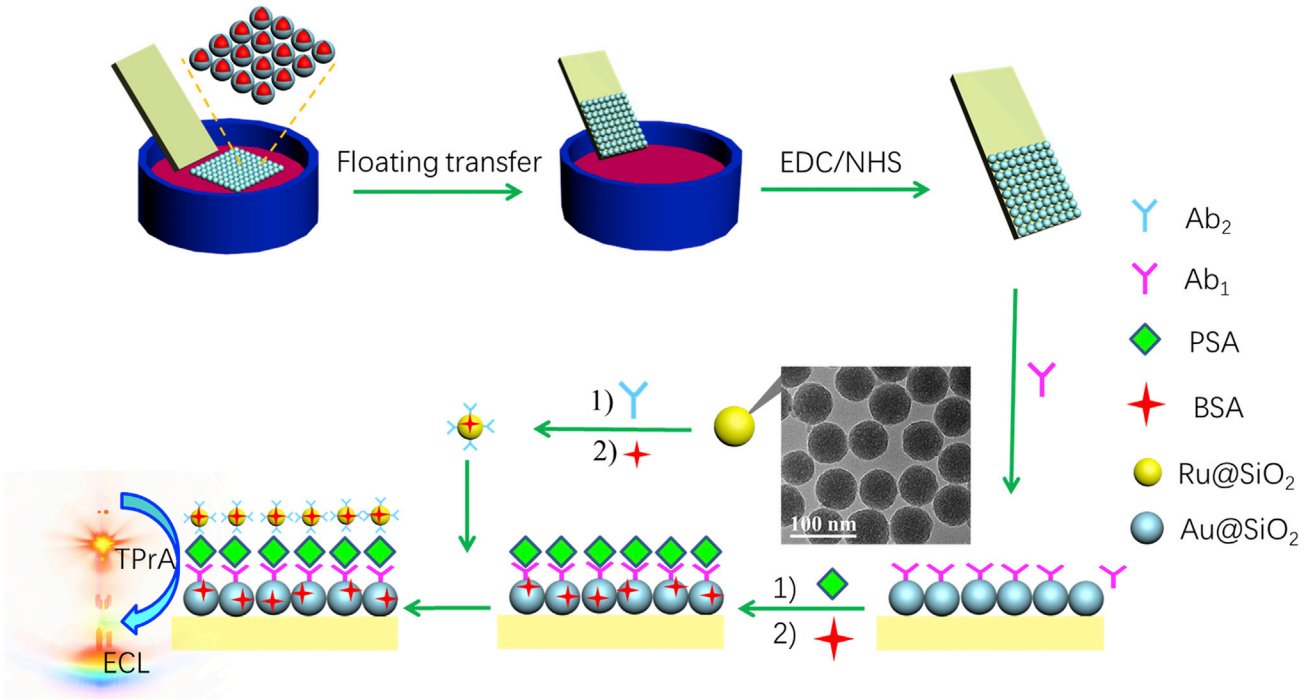

Scheme 1. Fabrication Procedures for the MASNE-Based PSA Immunosensors

As clearly seen in Figure 3D, the ECL intensity increases with an increase in silica shell thickness. However, with further increase of the silica shells the ECL intensity of the resulting MASNE decreases. Experimentally, when the shell thickness is ~21.5±1.7 nm, the ECL intensity of the MASNE system reaches the highest value (~1.6×10^4 a.u.), which is up to 1,000-fold enhancement than that of bare ITO (Figure 3D). Comparison ECL experiments by using $Ru@SiO_2$ as luminophore instead of $Ru(bpy)_3^{2+}$ solution to avoid the influence of quenching effect of bare AuNPs to $Ru(bpy)_3^{2+}$ were also conducted. As shown in Figure S6, although the ECL enhancement is slightly smaller than that in $Ru(bpy)_3^{2+}$ solution due to further increase of average distance (≥ 21.5 nm) between the embedded $Ru(bpy)_3^{2+}$ in $Ru@SiO_2$ NPs and the Au@21.5 nm SiO_2 NPs, the ECL intensity of the 75-nm Au@21.5 nm SiO_2 NP-modified ITO was still much higher than that of bare ITO and the 75-nm AuNP-modified ITO, which further demonstrated the superior performance of the Au@SiO_2-modified ECL electrodes. However, due to the quenching effect induced between AuNPs and the embedded $Ru(bpy)_3^{2+}$ in $Ru@SiO_2$, the ECL intensity of AuNP-modified electrode is still lower than that of bare ITO. This is because ECL emission is a competing result of two effects: one is the quenching effect induced by energy transfer between the luminophores and AuNPs and the other is PIRET enhancement. When AuNPs approach to $Ru(bpy)_3^{2+}$ closely, non-radiative energy transfer plays an important role and then the ECL intensity enhancement is very limited. With the increase of SiO_2 shell thickness, energy transfer between the $Ru(bpy)_3^{2+}$ and AuNPs decrease rapidly, thus non-radiative energy transfer can be effectively prevented and the radiative mode dominates, resulting in significant ECL enhancement (Li et al., 2018). However, further increase in the thickness of SiO_2 shell will cause an exponential decay of the EM field with distance, which in turn decreases the ECL intensity. The plasmonic effects on the ECL enhancement were implied because the ECL response of the control (AuNP-free) monolayer SiO_2 nanomembrane electrode (detailed characterization see Figure S7) showed only ~9-fold enhancement than that of the bare ITO electrode due to "nanoelectrode" surface effect (which increases the effective surface area of the electrode) and the enrichment of $Ru(bpy)_3^{2+}$ (Wang et al., 2015a) in this case (Figure S8).

The plasmonic nature of the fabricated MASNE was further manifested by *in situ* dark-field scattering imaging. As seen from Figure S9, the metasurface of the MASNE showed intense plasmonic scattering of yellow-green color. Upon the generation of excited $Ru(bpy)_3^{2+*}$ via electrochemical reaction, ECL emission excites surface plasmons optically on the metasurface, due to the spectral overlap between the LSPR band of $Au@SiO_2$ and the spectrum of $Ru(bpy)_3^{2+}$ (Figure 3E). Upon resonant excitation, the LSPR on the

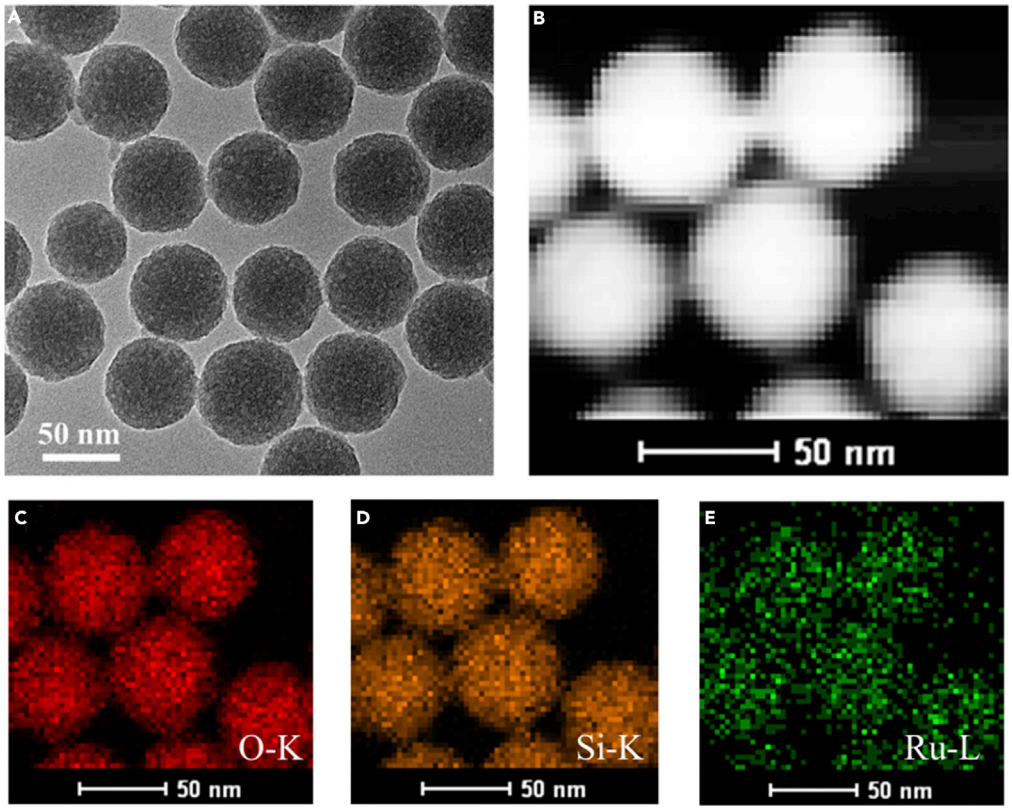

Figure 4. Morphological Characterizations of the Ru@SiO_2 NPs

(A–E) (A) Transmission electron microscopic image, (B) high-angle annular dark-field scanning transmission electron microscopic image, and (C–E) the corresponding energy-dispersive X-ray spectroscopic elemental mappings of Ru@SiO_2 NPs.

electrode surface breaks the diffraction limit and can concentrate light down to a nanoscale region (Jiang et al., 2014); the strong light localization makes the optical electric field near the metasurface largely enhanced, which is consistent with the FDTD simulation in Figure 1A (up to 15-fold). Figure S10 shows the simulated excitation wavelength-dependent EM field enhancement of the metasurface. The results indicated that the 550-nm excitation light results in a higher EM field enhancement when compared with 450- and 700-nm incident light, which is consistent with the LSPR spectra of the Au@SiO_2 nanomembrane. This kind of strong EM field enhancement and near-field dipole-dipole LSPR coupling could increase both the excitation rate and emission factor of $Ru(bpy)_3^{2+}$, resulting in significant enhancement in the ECL intensity.

To prove this conjecture, we studied the ECL intensity variation with the decrease of AuNP core sizes (while keeping the silica shell as a constant, ~21 nm; see Figures S11 and S12 for detailed characterization of Au@SiO_2). It is worth noting that because simultaneous cyclic voltammetry (CV) characterizations of the different ECL electrodes were nearly identical (See Figure S13), the observed ECL signal difference was not a main reflection of the change of surface area caused by different Au@SiO_2 preparations. As seen from Figures 3F and S14, smaller AuNPs result in lower ECL intensity (~13,600 a.u. and 9,920 a.u. for 50- and 20-nm AuNPs, respectively); this is because smaller AuNP cores generate weaker near-EM field, which is consistent with our prediction (FDTD simulation, see Figures 1B and 1C). Furthermore, the 2D well-organized metasurface we fabricated has large aspect ratio and is favorable for light scattering. As seen from Figure S15, the ECL intensity of the ordered metasurface is much stronger than that of the disordered structures (for detailed SEM images of the disordered structures see Figure S16); this elastic scattering by plasmons is the source of the EM enhancement contribution, and the enhanced re-radiated dipolar fields in turn excites the ECL emission of molecules (Atwater and Polman, 2010; Li et al., 2013). Thus the ECL emission can be effectively enhanced. All the results presented above indicated that the strong localized EM field and LSPR coupling

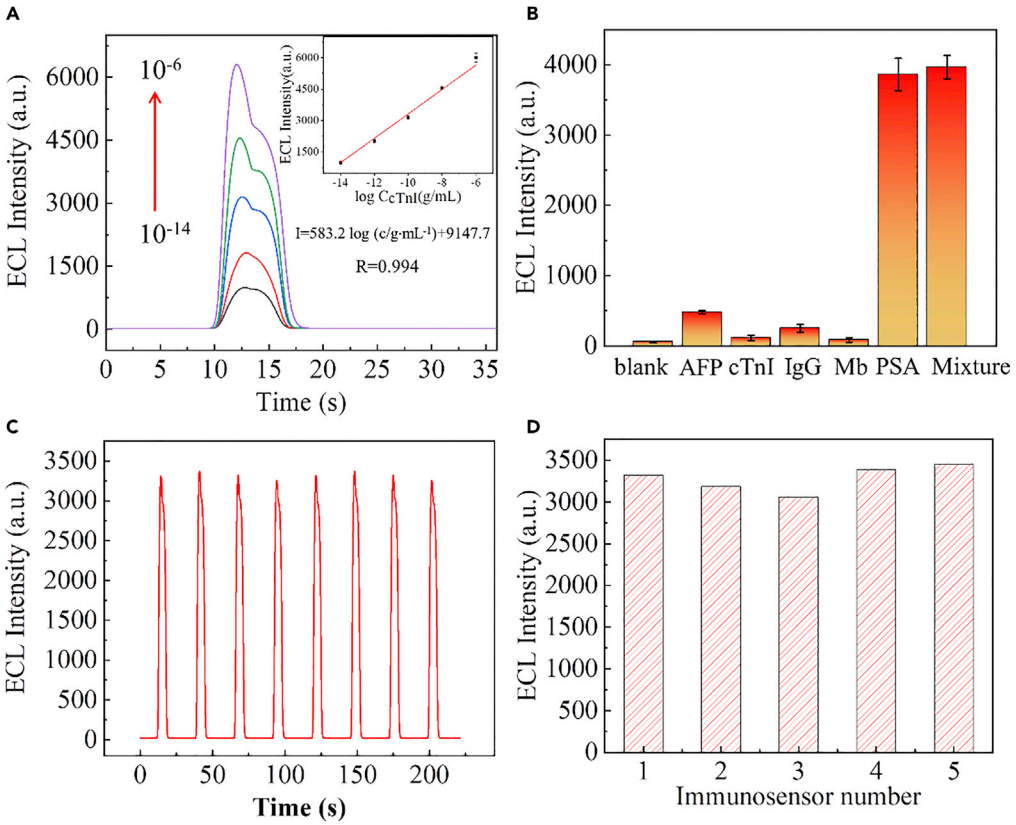

Figure 5. Detection Performance of the Constructed PSA ECL Immunosensor

(A) Linear relationship between the ECL intensity and PSA concentrations.

(B) Selectivity of the ECL immunosensor: blank, AFP (10 ng mL^{-1}), cTnI (10 ng mL^{-1}), IgG (10 ng mL^{-1}), Mb (10 ng mL^{-1}), PSA (1 ng mL^{-1}), and mixture (containing all the above analytes). AFP, alpha-fetoprotein; cTn1, cardiac troponin I; IgG, immunoglobulin G; Mb, myoglobin.

(C) Stabilization of the ECL emission (0.1 nM).

(D) Reproducibility of five independent immunosensors (0.1 nM).

See also Figures S17, Table S1.

(collective wave-like charge density fluctuation and surfing of electrons) play a crucial role in the metasurface-mediated huge ECL enhancement. In addition, the high-density of "hot spots" in the nanogaps between two adjacent Au@SiO_2 NPs also played a key role in the improvement of ECL enhancement.

The applicability and detection performance of the as-prepared (MASNE) metasurfaced ECL biosensors were further examined by applying for PSA detection. A schematic diagram of the MASNE ECL biosensor for PSA detection is shown in Scheme 1 (for detailed CV characterizations after every modification step see Figure S17). First, the primary antibody to PSA (Ab_1) was immobilized on the surface of an MASNE electrode with 1-ethyl 3-(3-(dimethylamino)propyl) carbodiimide hydrochloride/n-hydroxysuccinimide (EDC/NHS), which provided specific binding sites for PSA. The Ab_1-modified MASNE electrode was then immersed into the secondary antibody (Ab_2)-decorated Ru@SiO_2 solution. In the presence of PSA, a sandwich-type PSA ECL immunosensor was formed. As the number of Ru@SiO_2 NPs (for detailed characterization see Figure 4) immobilized on the surface of MASNE electrode is proportional to the PSA concentration (signal-on), the proposed detection method could be used for quantitative determination of PSA. As shown in Figure 5A, the intensity of ECL increased with the increase of PSA concentration until the binding saturation is reached, which indicated that the prepared ECL immunosensor was appropriate and reliable for PSA detection. In addition, the ECL intensity increased linearly with the logarithm of PSA concentration ranging from 10 fg mL^{-1} to 1 μg mL^{-1} with a regression equation of I = 583.2log (c/g mL^{-1}) + 9147.7 and a correlation coefficient of 0.994 (n = 3). Under the optimized condition, a limit of detection of 3 fg mL^{-1} (S/N = 3) was obtained (Gao et al., 2017), which is much lower (or comparable) than those

Sample Number	Added ($ng \cdot mL^{-1}$)	Found ($ng \cdot mL^{-1}$)	Recovery (%)
1	10	9.63	96.3%
2	0.1	0.0951	95.1%
3	0.001	0.001076	107.6%

Table 1. Quantitative Determination of PSA in Healthy Human Serum Sample

previously reported by other methods, especially for the reported sandwich-type PSA ECL biosensors (Table S1). To evaluate the practical application of the prepared PSA SEECL immunosensor, the selectivity was performed by introducing alpha-fetoprotein (AFP), cardiac troponin I (cTnI), immunoglobulin G (IgG), and myoglobin (Mb) as interfering proteins into the detection system.

The concentration of the interfering proteins was chosen as 10 ng mL^{-1} (much higher than those in healthy people's serum to ensure that it met with the testing requirements of actual samples), whereas the concentration of PSA was set as 1 ng mL^{-1}. As shown in Figure 5B, only the presence of PSA led to an obvious ECL enhancement, whereas the ECL responses of the interfering proteins showed almost no difference compared with the blank solution. These results demonstrated that the developed metasurfaced SEECL immunosensor had a good selectivity for PSA detection. Moreover, as seen from Figures 5C and 5D, the PSA SEECL biosensor showed very stable ECL intensity and reproducibility (the relative standard deviation of the tested five ECL electrodes were ~5%), which indicated the reliability of the immunosensor for ECL PSA detection. To further assess the practicability of the as-proposed immunosensor, standard addition method was applied to analyze the PSA concentrations in human serum. The detecting solution was prepared by adding PSA of different concentrations (10, 0.1, 0.001 ng mL^{-1}) into diluted serum samples. As shown in Table 1, the as-fabricated PSA SEECL biosensors showed great performance with a recovery of 95.1%–107.6%. The results identified the feasibility of the SEECL immunosensor for promising clinical ultrasensitive detection of PSA.

Conclusion

In summary, we developed a superior ECL-sensing platform by surface decoration of ECL electrodes with a dense monolayered metamaterial nanomembrane, made by self-assembly of plasmonic and size-tunable Au@SiO_2 NPs. The finely prepared metasurfaced ECL electrode with well-controlled core/shell sizes and interparticle spacing supports simultaneously photonic enhancement (resonant light scattering), PIRET, and silica shell-mediated "hot spot" effect, enhancing synergistically the ECL efficiency. The optimized metasurface electrode showed over 1,000-fold ECL enhancement for the classical $Ru(bpy)_3^{2+}$-TPrA system, which is the highest ECL enhancement ever reported. The as-fabricated metasurfaced ECL biosensor demonstrated superior detection performance in detecting cancer biomarker PSA with a detection limit of 3 fg mL^{-1}. This work provides a new insight into the understanding of full utilization of plasmonic effects on ECL and opens a way to design a high-performance ECL-sensing platform for ultrasensitive bioassays.

Limitations of the Study

As the arrangement of NPs plays an important role in the performance of biosensors, 2D nanomembrane with poor quality may not result in superior (up to 1,000-fold) enhancement.

METHODS

All methods can be found in the accompanying Transparent Methods supplemental file.

SUPPLEMENTAL INFORMATION

Supplemental Information can be found online at https://doi.org/10.1016/j.isci.2019.06.042.

ACKNOWLEDGMENTS

C.L. thanks Prof. Guobao Xu for helpful discussion of the manuscript. Y.J. acknowledges support by the Natural Science Foundation of China (Grant Nos. 21675146 and 21475125), the National Key Research and Development Program of China (Grant No. 2016YFA0201300), and the Instrument Developing Project of the Chinese Academy of Sciences (Grant No. YZ201666).

AUTHOR CONTRIBUTIONS

Y.J. and C.L. conceived and designed the project. C.L. prepared the metamaterials, conducted the structural and optical characterizations, and fabricated the immunosensor. S.W. performed the ECL experiments. C.L., S.W., M.S., H.L., C.X., and Y.J. analyzed and discussed the data. Y.J., H.L., and C.L. wrote the paper.

DECLARATION OF INTERESTS

The authors declare no competing interests.

Received: April 25, 2019
Revised: June 3, 2019
Accepted: June 28, 2019
Published: July 26, 2019

REFERENCES

Atwater, H.A., and Polman, A. (2010). Plasmonics for improved photovoltaic devices. Nat. Mater. *9*, 205.

Burokur, S.N., Daniel, J.-P., Ratajczak, P., and de Lustrac, A. (2010). Tunable bilayered metasurface for frequency reconfigurable directive emissions. Appl. Phys. Lett. *97*, 064101.

Gao, W., Qi, L., Liu, Z., Majeed, S., Kitte, S.A., and Xu, G. (2017). Efficient lucigenin/thiourea dioxide chemiluminescence system and its application for selective and sensitive dopamine detection. Sens. Actuators B *238*, 468–472.

Hu, L., and Xu, G. (2010). Applications and trends in electrochemiluminescence. Chem. Soc. Rev. *39*, 3275–3304.

Jain, P.K., Huang, X., El-Sayed, I.H., and El-Sayed, M.A. (2008). Noble metals on the nanoscale: optical and photothermal properties and some applications in imaging, sensing, biology, and medicine. Acc. Chem. Res. *41*, 1578–1586.

Jebb, M., Sudeep, P.K., Pramod, P., Thomas, K.G., and Kamat, P.V. (2007). Ruthenium(II) trisbipyridine functionalized gold nanorods. morphological changes and excited-state interactions. J. Phys. Chem. B *111*, 6839–6844.

Jiang, R., Li, B., Fang, C., and Wang, J. (2014). Metal/semiconductor hybrid nanostructures for plasmon-enhanced applications. Adv. Mater. *26*, 5274–5309.

Li, J., Cushing, S.K., Zheng, P., Meng, F., Chu, D., and Wu, N. (2013). Plasmon-induced photonic and energy-transfer enhancement of solar water splitting by a hematite nanorod array. Nat. Commun. *4*, 2651.

Li, L., Chen, Y., and Zhu, J.-J. (2017). Recent advances in electrochemiluminescence analysis. Anal. Chem. *89*, 358–371.

Li, M.-X., Feng, Q.-M., Zhou, Z., Zhao, W., Xu, J.-J., and Chen, H.-Y. (2018). Plasmon-enhanced electrochemiluminescence for nucleic acid detection based on gold nanodendrites. Anal. Chem. *90*, 1340–1347.

Li, M.-X., Zhao, W., Qian, G.-S., Feng, Q.-M., Xu, J.-J., and Chen, H.-Y. (2016). Distance mediated electrochemiluminescence enhancement of CdS thin films induced by the plasmon coupling of gold nanoparticle dimers. Chem. Commun. (Camb.) *52*, 14230–14233.

Lin, L., Zapata, M., Xiong, M., Liu, Z., Wang, S., Xu, H., Borisov, A.G., Gu, H., Nordlander, P., Aizpurua, J., et al. (2015). Nanooptics of plasmonic nanomatryoshkas: shrinking the size of a core–shell junction to subnanometer. Nano Lett. *15*, 6419–6428.

Liu, Z., Qi, W., and Xu, G. (2015). Recent advances in electrochemiluminescence. Chem. Soc. Rev. *44*, 3117–3142.

Lu, H.-J., Pan, J.-B., Wang, Y.-Z., Ji, S.-Y., Zhao, W., Luo, X.-L., Xu, J.-J., and Chen, H.-Y. (2018). Electrochemiluminescence energy resonance transfer system between RuSi nanoparticles and hollow Au nanocages for nucleic acid detection. Anal. Chem. *90*, 10434–10441.

Miao, W. (2008). Electrogenerated chemiluminescence and its biorelated applications. Chem. Rev. *108*, 2506–2553.

Richter, M.M. (2004). Electrochemiluminescence (ECL). Chem. Rev. *104*, 3003–3036.

Shin, Y., Song, J., Kim, D., and Kang, T. (2015). Facile preparation of ultrasmall void metallic nanogap from self-assembled gold–silica core–shell nanoparticles monolayer via kinetic control. Adv. Mater. *27*, 4344–4350.

Wang, D., Guo, L., Huang, R., Qiu, B., Lin, Z., and Chen, G. (2015a). Surface enhanced electrochemiluminescence of $Ru(bpy)_3^{2+}$. Sci. Rep. *5*, 7954.

Wang, D., Li, Y., Lin, Z., Qiu, B., and Guo, L. (2015b). Surface-enhanced electrochemiluminescence of $Ru@SiO_2$ for ultrasensitive detection of carcinoembryonic antigen. Anal. Chem. *87*, 5966–5972.

Wang, J., Shan, Y., Zhao, W.-W., Xu, J.-J., and Chen, H.-Y. (2011). Gold nanoparticle enhanced electrochemiluminescence of CdS thin films for ultrasensitive thrombin detection. Anal. Chem. *83*, 4004–4011.

Wu, N. (2018). Plasmonic metal–semiconductor photocatalysts and photoelectrochemical cells: a review. Nanoscale *10*, 2679–2696.

Wu, P., Hou, X., Xu, J.-J., and Chen, H.-Y. (2014). Electrochemically generated versus photoexcited luminescence from semiconductor nanomaterials: bridging the valley between two worlds. Chem. Rev. *114*, 11027–11059.

Zhang, J., Gryczynski, Z., and Lakowicz, J.R. (2004). First observation of surface plasmon-coupled electrochemiluminescence. Chem. Phys. Lett. *393*, 483–487.

ISCI, Volume *17*

Supplemental Information

Nanoengineered Metasurface Immunosensor with over 1000-Fold Electrochemiluminescence Enhancement for Ultra-sensitive Bioassay

Chuanping Li, Shanshan Wang, Haijuan Li, Muhammad Saqib, Chen Xu, and Yongdong Jin

Supplemental Information

Core/Shell/Gap-Nanoengineered Metasurface Immunosensor with over 1000-Fold Electrochemiluminescence Enhancement for Ultra-sensitive Bioassay

Chuanping Li[1,2,4,5], Shanshan Wang[1,3,5], Haijuan Li[1], Muhammad Saqib[1], Chen Xu[1] & Yongdong Jin[1,2,*]

[1]State Key Laboratory of Electroanalytical Chemistry, Changchun Institute of Applied Chemistry, Chinese Academy of Sciences, 5625 Renmin Street, Changchun 130022, P. R. China.

[2] University of Chinese Academy of Sciences, Beijing 100049, P. R. China.

[3] College of Chemistry, Liaoning University, Shenyang 110036, P. R. China.

[4] current address: College of Biological and Chemical Engineering, Anhui Polytechnic University, Wuhu 241000, P. R. China.

[5] These authors contributed equal to this work.

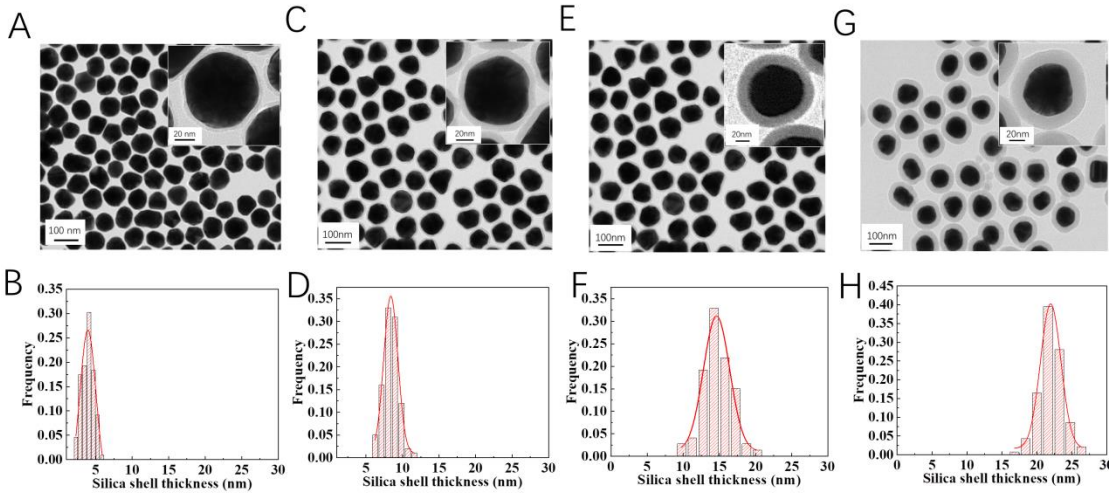

Figure S1. TEM images and silica shell thicknesses distributions of 75 nm Au@SiO_2 NPs. (A-B) 75 nm Au@4.0 ± 0.8 nm SiO_2 NPs, (C-D) 75 nm Au@8.4 ± 1.1 nm SiO_2 NPs, (E-F) 75 nm Au@14.9 ± 2.0 nm SiO_2 NPs, (G-H) 75 nm Au@24.6 ± 2.7 nm SiO_2 NPs. Data are represented as mean $\pm$ TEM. Related to Figure 2.

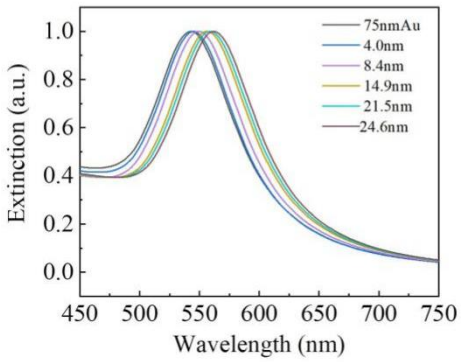

Figure S2. UV-Vis spectra of the 75 nm Au@SiO_2 NPs. Related to Figure 2.

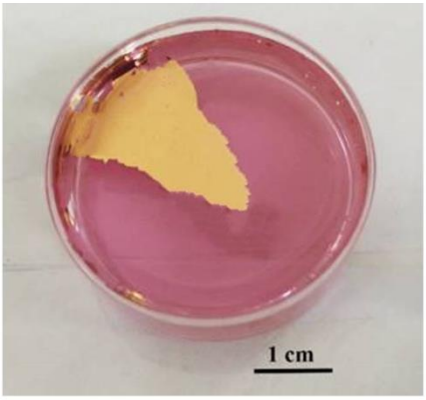

Figure S3. Photograph of the monolayered 75 nm Au@21.5 nm SiO_2 nanomembrane. Related to Figure 2.

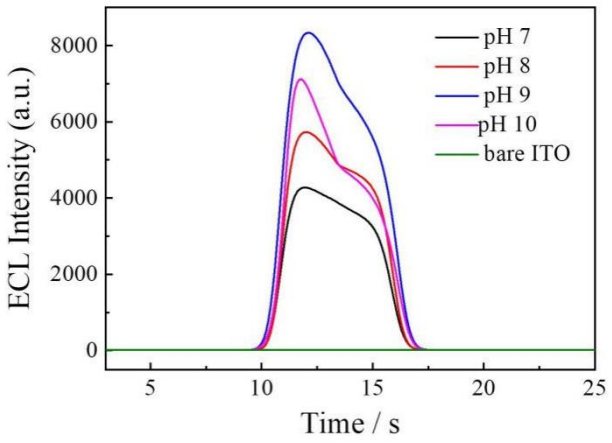

Figure S4. ECL intensity of the 75 nm Au@21.5 nm SiO_2 modified MASNE at 0.1 M PBS solution (containing 20 μM $Ru(bpy)_3^{2+}$ and 0.1 mM tri-n-propylamine (TPrA)) with different pH value. Related to Figure 3.

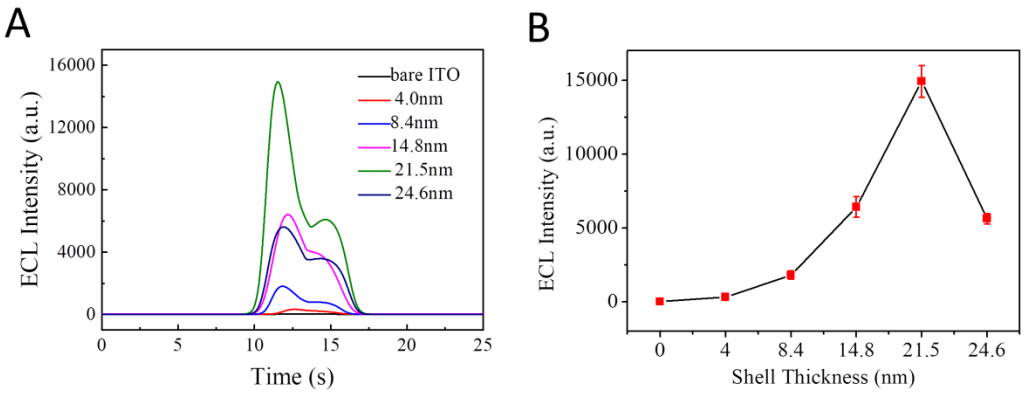

Figure S5. ECL intensity of the 75 nm Au@ SiO_2 modified MASNE with different silica shell thicknesses (0.1 M PBS solution (pH=9) containing 20 μmol L^{-1} $Ru(bpy)_3^{2+}$ and 0.1 mmol L^{-1} TPrA). Related to Figure 3.

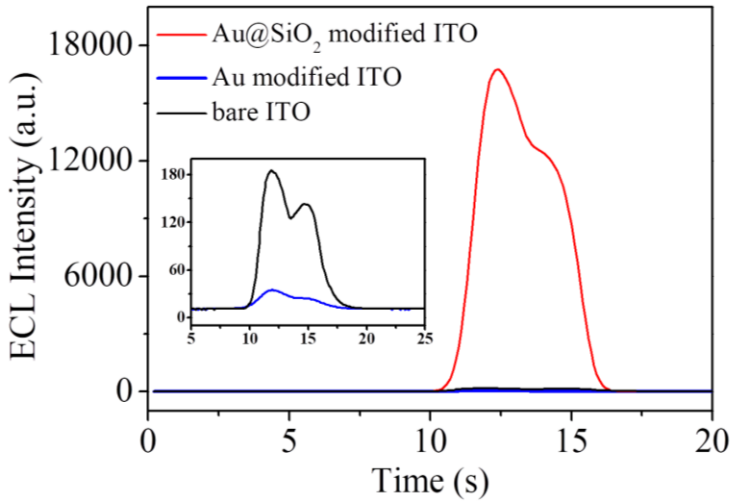

Figure S6. The comparison of ECL intensity between 75nm Au@21.5 nm SiO_2 NPs and 75 nm AuNPs fabricated ECL electrodes using Ru@SiO_2 as luminophore. Inset: enlarged image of ECL intensity of Au modified ITO and bare ITO electrode. Related to Figure 3.

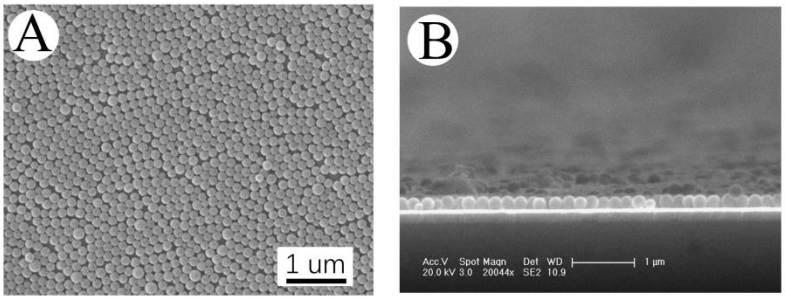

Figure S7. SEM images of the fabricated monolayered SiO_2 nanomembrane-based ECL electrode. (A) Top view, (B) Side view of the SEM image. Related to Figure 3.

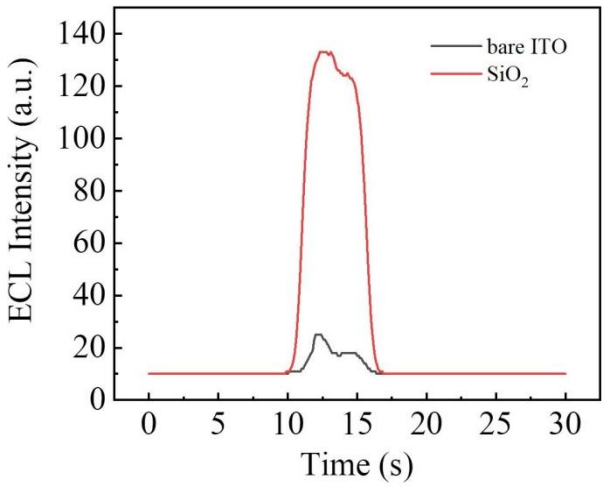

Figure S8. ECL intensity of bare SiO_2NPs fabricated MASNE in 0.1 M PBS (pH=9) buffer containing 20 µ M $Ru(bpy)_3^{2+}$ and 0.1 mM tripropylamine (TPrA). Related to Figure 3.

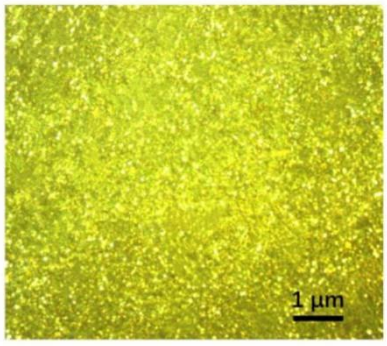

Figure S9. Microscopy-based selected area dark field scattering image of the MASNE constructed with 75 nm Au@21.5 nm SiO_2 NPs. Related to Figure 3.

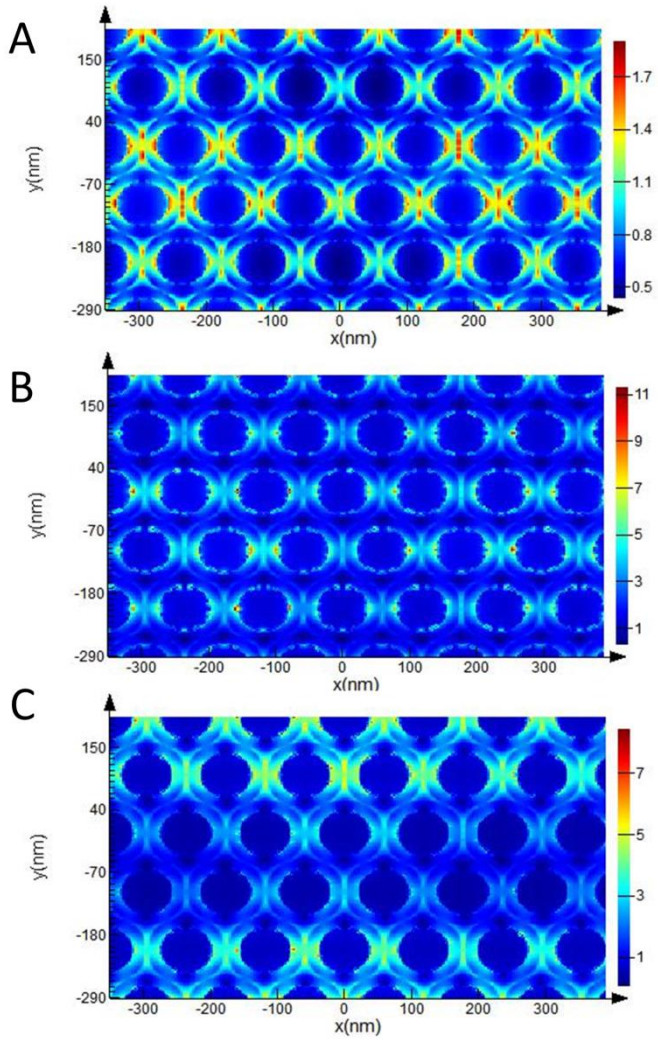

Figure S10. Wavelength dependent EM field enhancement with excitation light of (A) 450 nm, (b) 550 nm, (c)700 nm**.** Related to Figure 3.

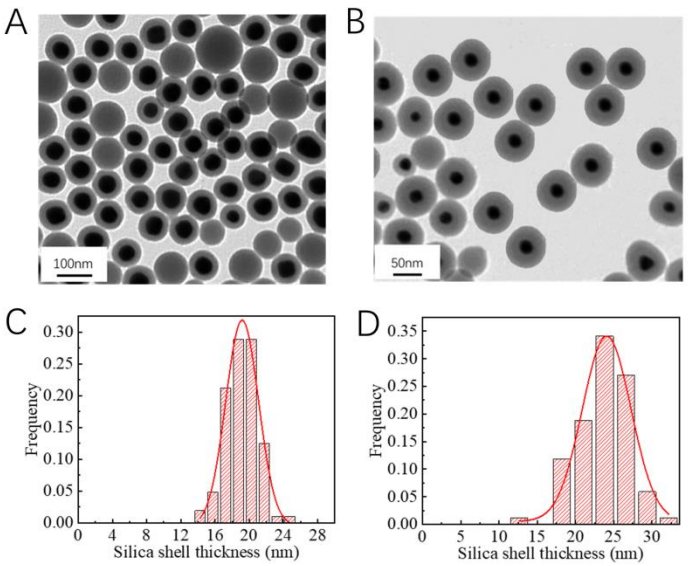

Figure S11. TEM images and silica shell thicknesses distributions of Au@SiO_2 NPs. (A, C) 50 nm Au@19.9±1.9 nm SiO_2. (B, D) 20 nm Au@22.5±3.2 nm SiO_2. Related to Figure 3.

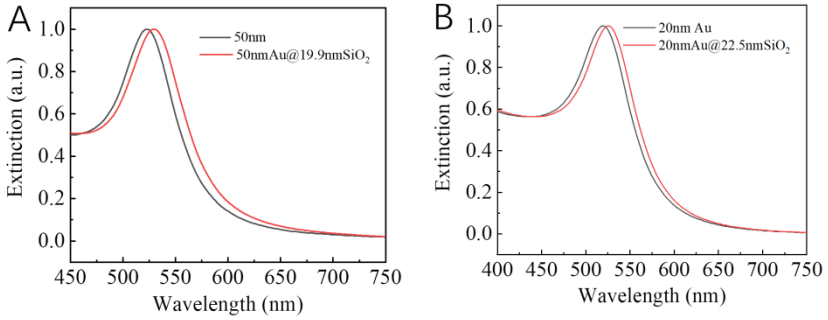

Figure S12. UV-Vis spectra of Au@SiO_2 NPs. (A) 50 nm Au@19.9±1.9 nm SiO_2. (B) 20 nm Au@22.5±3.2 nm SiO_2. Related to Figure 3.

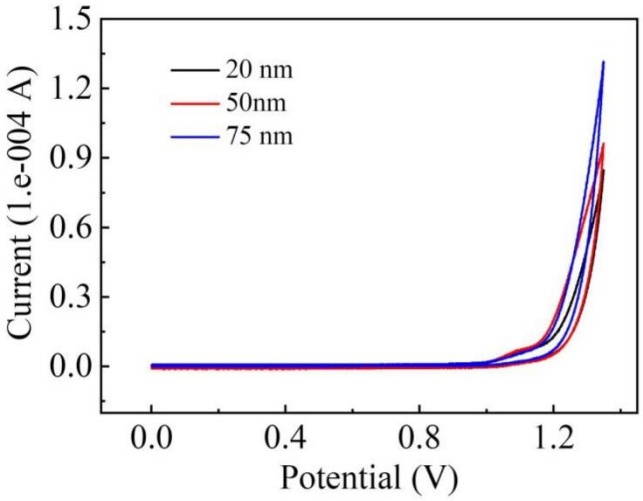

Figure S13. Simultaneous electrochemical measurements of ECL electrodes modified with different Au@21.5 nm SiO_2 NPs. Related to Figure 3.

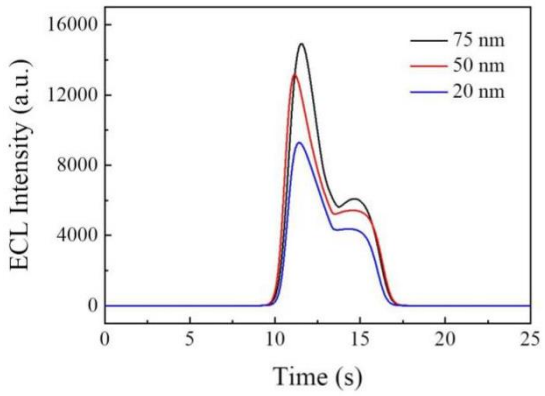

Figure S14. The ECL intensity of the Au@21.5 nm SiO_2-based MASNEs with different AuNPs sizes in 0.1 M PBS (pH=9) buffer containing 20 μM $Ru(bpy)_3^{2+}$ and 0.1 mM tripropylamine (TPrA). Related to Figure 3.

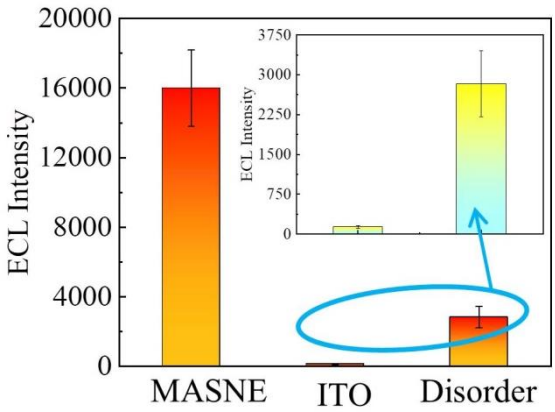

Figure S15. Comparation of ECL intensity between 75 nm Au@21.5 nm SiO_2 NPs-based MASNE, ITO and disorderly stacked 75 nm Au@21.5 nm SiO_2 NPs fabricated ECL electrode. Related to Figure 3.

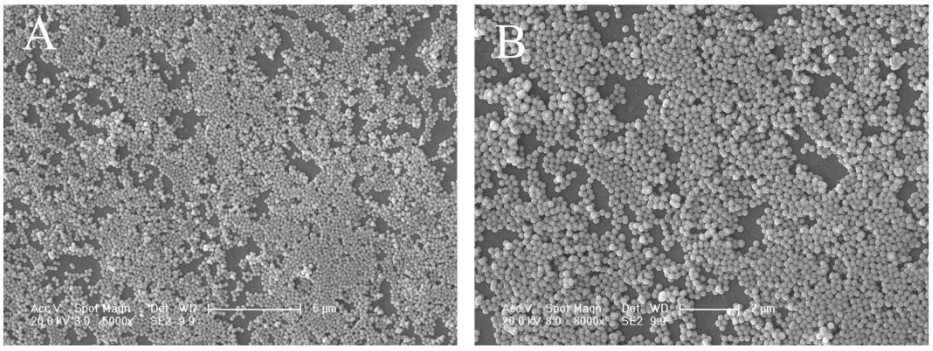

Figure S16. SEM images of the disordered Au@SiO_2 fabricated ECL electrode. Related to Figure 3.

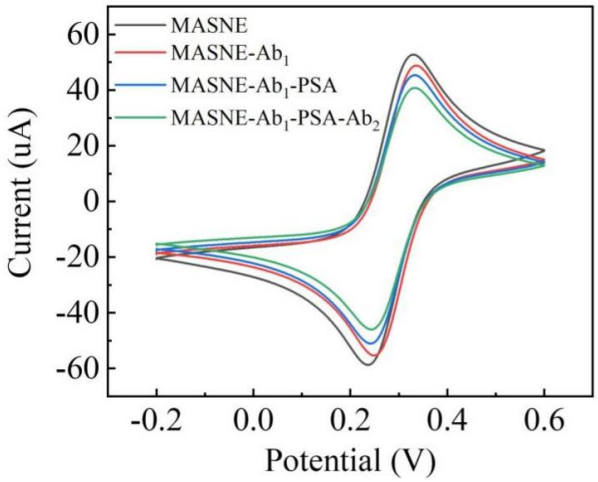

Figure S17. Cyclic voltammograms (in 2 mM $K_3Fe(CN)_6$ solution, sweep rate 50 mV/s) for the ECL sensing platform during the fabrication. Compared with the bare MASNE, the peak current decreases after every modification step because of the poor conductivity of the biomolecules and Ru@SiO_2. Related to Figure 5.

Table S1. Comparison of ECL immunosensor with other reported immunosensors for determination of PSA. Related to Figure 5.

methods	linear range	detection limit	reference
electrochemical	-	0.9 pg mL^{-1}	(Zheng et al., 2005)
enzyme-linked immunosorbent assay	-	14 fg mL^{-1} (0.4 fM)	(Rissin et al., 2010)
electrochemical	0.4-40 ng mL^{-1}	4 pg ml^{-1}	(Yu et al., 2006)
SERS	5.0 pg mL^{-1}-50 ng mL^{-1}	0.012 ng mL^{-1}	(Cheng et al., 2017)
Bio-bar-code assay	-	0.003-0.03 fM	(Nam et al., 2003)
ECL	0.5-500 ng mL^{-1}	0.058 ng mL^{-1}	(Shao et al., 2018)
ECL	5.0 pg mL^{-1}-5.0 ng mL^{-1}	0.8 pg mL^{-1}	(Qi et al., 2014)
ECL	10 fg mL^{-1}-1 μg mL^{-1}	3 fg mL^{-1}(~0.1 fM)	This work

Transparent Methods

Materials

3-Aminopropyltrimethoxysilane (APTMS), Tri(2,2'-bipyridyl)dichlororuthenium (Ⅱ) hexahydrate ($Ru(bpy)_3Cl_2,6H_2O$), Sodium citrate (Na_3CA), Tripropylamine (TPrA), sodium silicate (Na_2SiO_3) were purchased from Sigma-Aldrich. $HAuCl_4·4H_2O$, methanol, n-hexane were purchased from Beijing Chemical Factory (Beijing, China). Tetraethyl orthosilicate (TEOS) and Triton X-100 (TX-100) were purchased from Aladdin Co., Ltd. ITO-coated glass was purchased from Zhuhai Kaivo Optoelectric Technology Co., Ltd. 3-(Triethoxysilyl)propylsuccinic anhydride was purchased from Innochem Co., Ltd. Bovine serum albumin (BSA), IgG, Mb, PSA, AFP, cTnI were purchased from Sinopharm Chemical Reagent Co. Ltd. (Beijing, China). All of the chemicals were used without further purification. Water used throughout all these experiments was purified with a Millipore system (18.2 MΩ· cm).

Characterization

The size and morphologies of the $Au@SiO_2$ NPs were characterized with a JEM-2100F transmission electron microscope (TEM) and scanning electron microscope (SEM) images were performed with an XL30 ESEM SEM. The UV−vis absorption spectra were obtained by a UV-2600 spectrophotometer (Shimadzu). Optical microscopy-based selected area dark-field scattering images and spectra were obtained by using an inverted Leica DMI6000B microscope (Germany), equipped with a Princeton spectrometer (PIXIS 256). The ECL experiments were performed on a MPI-A multifunctional electrochemical and chemiluminescent analytical system (Xi'An Remax Electronic Science & Technology Co. Ltd., 350-650 nm). The voltage of the photomultiplier tube (PMT) was set at 500 V. The experiments were carried out with a conventional three-electrode system. The working, counter and reference electrodes were ITO electrode, Pt wire and Ag/AgCl electrode, respectively.

Synthesis of $Au@SiO_2$ NPs

The AuNPs with different size were synthesized by the methods reported elsewhere.(Frens, 1973; Haiss et al., 2007) $Au@SiO_2$ NPs of different silica shell

thicknesses were synthesized by the method reported by Tian's group and our previous work (Li et al., 2010) with minor modification. Typically, 700 μL of fresh prepared 1 mM APTMS was drop-wise added to 30 mL of 75 nm gold sol and stirred for 20 min vigorously; then about 4 mL of 0.54% Na_2SiO_3 and 100 μL of 0.1 M H_2SO_4 was added in the mixture and heated at 90 ℃ for a period of time. After cooling to the room temperature, the nanoparticles were centrifuged at 4000 rpm for 18 min and diluted to 10 mL with deionized water. Au@SiO_2 NPs with tunable shell-thickness (4~8 nm) can be obtained by carefully controlling the reaction time, pH and concentration. In order to further increase the silica shell thickness, 10 mL Au@8 nm SiO_2NPs obtained were added to a mixture of 40 mL ethyl alcohol and 600 μL NH_3 H_2O, then a certain amount of 1% TEOS were added. After stirring at room temperature for 12, 24, 36 h, Au@SiO_2 NPs with silica shell thicknesses of ~15, ~22 and ~25 nm were obtained respectively.

Modification of Au@SiO_2 NPs

In order to improve the quality of the self-assembled nanomembrane, Au@SiO_2 NPs with silica shell thicknesses of ~15 nm, ~22 nm, ~25 nm were carboxylated with 3-(Triethoxysilyl)propylsuccinic anhydride by the following steps. Firstly, the as-prepared Au@SiO_2 NPs were centrifuged at 5000 rpm three times and diluted with isopropanol. Then, 0.5 mL of 10 mM 3-(Triethoxysilyl)propylsuccinic anhydride were added and heated at 85℃ for 24 h. Finally, the nanoparticles were centrifuged at 6000 rpm for three times and diluted with deionized water to 10 mL.

Fabrication of monolayered Au@SiO_2 nanomembrane-based ECL electrode (MASNE)

ITO glass was firstly cleaned with sonication in water, acetone, ethyl alcohol and finally in water for 10 min, respectively. Then, each slide was placed in a solution of 5:1:1 H_2O + 30% H_2O_2+25% NH_3 and heated at 80 ℃ for about 20 min. Finally, the ITO glasses were dried with N_2. The monolayer Au@SiO_2 nanomembranes were prepared by a method of liquid/liquid interface self-assembly (LLISA). Typically, 3 mL of Au@SiO_2 NPs was added to a plastic container, then 460 μL of n-hexane was added to form a two-phase interface. Then, 3.7 mL of methanol was poured rapidly

into the mixture to capture the nanoparticles at the hexane/water interface. After the evaporation of hexane, the nanoparticles were simultaneously self-assembled into a monolayer over a large area (up to several cm^2) at the water/hexane interface. Then the nanomembranes were transferred carefully from the "soft" air−water interface onto the ITO electrodes as depicted in our method reported elsewhere. (Wu et al., 2016) The disordered nanomembranes-based ECL electrode was prepared by a dropping method with the same amount of $Au@SiO_2$ NPs.

Preparation and modification of $Ru@SiO_2$ nanoparticles

Based on the previous studies (Dong et al., 2016; Zhang and Dong, 2006), $Ru@SiO_2$ nanoparticles were prepared as follows: First, 1.80 mL of Triton X-100 were mixed with 7.5 mL of cyclohexane, 340 μL of 40 mM $Ru(bpy)_3^{2+}$ and 1.8 mL of n-hexanol. After stirring for 30 min, 0.1 mL of TEOS was added into the solution. Then, the polymerization reaction was started by adding 60 μL of $NH_3 \cdot H_2O$. The solution was stirred for 24 h to obtain $Ru@SiO_2$ NPs, which were isolated by acetone, and followed by centrifuging and washing with isopropanol. The precipitation was dispersed with isopropanol to a final volume of 15 mL. In order to carboxylate the surface of $Ru@SiO_2$ NPs, 62 mg of 3-(Triethoxysilyl)propylsuccinic anhydride were added and heated at 85℃ for 24 h. Finally, the nanoparticles were centrifuged at 8000 rpm for three times and diluted with deionized water to 15 mL.

Modification of $Ru@SiO_2$ NPs with Ab_2.

1 mL of $Ru@SiO_2$ NPs were mixed with 400 μL EDC (0.35 M) and NHS (0.1 M) solution for 40 min under stirring. Subsequently, 200 μL of Ab_2 (0.1 mg/mL) were added and stirred for 12 h at room temperature. Finally, the mixture was centrifuged and washed two times with water. Then the mixture was blocked by BSA solution for 1 h at room temperature, and thereafter centrifuged at 8000 rpm for 15 min. The precipitation was dispersed into 2 mL of 0.01M PBS (pH 7.4).

Fabrication of the PSA ECL biosensor

Firstly, a MASNE was added into the mixture solution containing 400 μL of EDC (0.35 M) and NHS (0.1 M) for 40 min. Then, 10 μL of Ab_1 (0.1 mg/mL) were dropped

on the MASNE and incubated for 2 h at 25℃. Subsequently, the MASNE was washed with 0.01 M PBS (pH 7.4) to remove the nonspecific absorption of Ab_1. The MASNE was then blocked with 3% BSA blocking solution for 2 h to block non-specific binding sites and washed with the washing buffer thoroughly. Next, 10 μL of PSA was dropped on the MASNE-Ab_1 and incubated for 2 h at 25℃. Thereafter, the decorated MASNE was washed with 0.01 M PBS (pH 7.4). At last, the decorated MASNE was incubated in the Ru@SiO_2-Ab_2 NP solution for 4 h, and then washed with the washing buffer. The ECL tests were performed in 0.1 M PBS (pH=7.4) containing 0.1 mM TPrA and the linear scan potential was applied from 0-1.35 V with a scan rate of 100 mV/s.

SUPPLEMENTAL REFERENCES

Cheng, Z., Choi, N., Wang, R., Lee, S., Moon, K.C., Yoon, S.-Y., Chen, L., and Choo, J. (2017). Simultaneous detection of dual prostate specific antigens using surface-enhanced raman scattering-based immunoassay for accurate diagnosis of prostate cancer. ACS Nano *11*, 4926-4933.

Dong, Y.-P., Chen, G., Zhou, Y., and Zhu, J.-J. (2016). Electrochemiluminescent sensing for caspase-3 activity based on $Ru(bpy)_3^{2+}$-doped silica nanoprobe. Anal. Chem. *88*, 1922-1929.

Frens, G. (1973). Controlled nucleation for the regulation of the particle size in monodisperse gold suspensions. Nature *241*, 20-22.

Haiss, W., Thanh, N.T.K., Aveyard, J., and Fernig, D.G. (2007). Determination of size and concentration of gold nanoparticles from UV−Vis spectra. Anal. Chem. *79*, 4215-4221.

Li, J.F., Huang, Y.F., Ding, Y., Yang, Z.L., Li, S.B., Zhou, X.S., Fan, F.R., Zhang, W., Zhou, Z.Y., Wu de, Y., *et al.* (2010). Shell-isolated nanoparticle-enhanced Raman spectroscopy. Nature *464*, 392-395.

Nam, J.-M., Thaxton, C.S., and Mirkin, C.A. (2003). Nanoparticle-based bio-bar codes for the ultrasensitive detection of proteins. Science *301*, 1884-1886.

Qi, H., Li, M., Dong, M., Ruan, S., Gao, Q., and Zhang, C. (2014). Electrogenerated chemiluminescence peptide-based biosensor for the determination of prostate-specific antigen based on target-induced cleavage of peptide. Anal. Chem. *86*, 1372-1379.

Rissin, D.M., Kan, C.W., Campbell, T.G., Howes, S.C., Fournier, D.R., Song, L., Piech, T., Patel, P.P., Chang, L., Rivnak, A.J., *et al.* (2010). Single-molecule enzyme-linked immunosorbent assay detects serum proteins at subfemtomolar concentrations. Nat. Biotechnol. *28*, 595.

Shao, K., Wang, B., Nie, A., Ye, S., Ma, J., Li, Z., Lv, Z., and Han, H. (2018). Target-triggered signal-on ratiometric electrochemiluminescence sensing of PSA based on MOF/Au/G-quadruplex. Biosens. Bioelectron. *118*, 160-166.

Wu, H., Li, C., Zhao, Z., Li, H., and Jin, Y. (2016). Free-standing monolayered metallic nanoparticle networks as building blocks for plasmonic nanoelectronic junctions. ACS Appl. Mater. Interfaces *8*, 1594-1599.

Yu, X., Munge, B., Patel, V., Jensen, G., Bhirde, A., Gong, J.D., Kim, S.N., Gillespie, J., Gutkind,

J.S., Papadimitrakopoulos, F., *et al.* (2006). Carbon nanotube amplification strategies for highly sensitive immunodetection of cancer biomarkers. J. Am. Chem. Soc. *128*, 11199-11205.

Zhang, L., and Dong, S. (2006). Electrogenerated chemiluminescence sensors using $Ru(bpy)_3^{2+}$ doped in silica nanoparticles. Anal. Chem. *78*, 5119-5123.

Zheng, G., Patolsky, F., Cui, Y., Wang, W.U., and Lieber, C.M. (2005). Multiplexed electrical detection of cancer markers with nanowire sensor arrays. Nat. Biotechnol. *23*, 1294.